

ARMY RESEARCH LABORATORY



Shear and Axial Stress Response Under Fixed-End Forward/Reverse Torsion Loading of OFHC Copper

by Tusit Weerasooriya

ARL-TR-1828

October 1998

19981127 083

Approved for public release; distribution is unlimited.

DTIC QUALITY INSPECTED 3

The findings in this report are not to be construed as an official Department of the Army position unless so designated by other authorized documents.

Citation of manufacturer's or trade names does not constitute an official endorsement or approval of the use thereof.

Destroy this report when it is no longer needed. Do not return it to the originator.

Army Research Laboratory

Aberdeen Proving Ground, MD 21005-5069

ARL-TR-1828

October 1998

Shear and Axial Stress Response Under Fixed-End Forward/Reverse Torsion Loading of OFHC Copper

Tusit Weerasooriya

Weapons and Materials Research Directorate, ARL

Abstract

Torsion tests are conducted under fixed-end (axial constraint) conditions on thin tubular OFHC copper specimens. After a large shear strain of 2.2 in the forward direction, the specimen is twisted back to zero shear strain. From the tests, shear and axial stresses are obtained as a function of shear strain. These stress responses are also obtained from the Taylor-type polycrystal analysis with simple shear boundary conditions. Single-crystal constitutive parameters in the polycrystal analysis are obtained from uniaxial compressive tests conducted for large strains. Experimental and predicted torsion test results are compared. The Taylor method predicts the experimental shear stress response reasonably well under simple shear boundary conditions. Most of the salient features of the experimental axial stress response are captured by the Taylor prediction.

Table of Contents

	<u>Page</u>
List of Figures	v
List of Tables	v
1. Introduction	1
2. Experimental Stress-Strain Behavior	3
2.1 Material	3
2.2 Experimental Procedure	3
2.3 Torsion Test Results	4
3. Polycrystal (Taylor) Model Prediction	6
3.1 Kinematics of the Single Crystal	7
3.2 Crystal Plasticity Constitutive Model	9
3.3 Numerical Procedure for Model Predictions	10
3.4 Model Predictions	13
4. Comparison of Experimental Results With Polycrystal Model Predictions	16
5. Summary and Conclusions	20
6. References	21
Distribution List	23
Report Documentation Page	27

INTENTIONALLY LEFT BLANK

List of Figures

<u>Figure</u>	<u>Page</u>
1. Experimental Shear and Sxial Stresses Plotted as a Function of Shear Strain	5
2. Magnitude of Experimental Shear Stresses Plotted as a Function of Total Shear Strain Showing a Small Bauschinger Effect	5
3. Experimental Axial Stress Plotted as a Function of Shear Strain	6
4. {111} Equal-Area Projection Pole Figures of Initial Randomly Oriented 100 Crystals.....	15
5. Predicted Shear, Axial, and Hoop Stresses as a Function of Shear Strain.....	16
6. Comparison of Experimental and Predicted Shear Stresses as a Function of Shear Strain	17
7. Magnitude of Experimental and Predicted Shear Stresses Plotted as a Function of Total Shear Strain.....	17
8. Experimental and Predicted Axial Stresses Plotted as a Function of Shear Strain....	18

List of Tables

<u>Table</u>	<u>Page</u>
1. Twelve Slip Systems for fcc Crystal.....	14

INTENTIONALLY LEFT BLANK

1. Introduction

During armor-antiarmor interaction, material elements at the interface are subjected to large deformations. These material elements reach large plastic strains and rotations monotonically and then undergo a large reversal of strain and rotation [1]. When numerically simulating such a finite deformation, predictions significantly depend on the constitutive models that represent the plastic deformation behavior. Constitutive models in most computer codes are extensions of the small plastic deformation behavior. In these codes, extension to multiaxiality is achieved through the assumption that there exists a unique effective stress-strain behavior for materials at a given strain rate and temperature. Finite strain deformation experiments show this assumption is not valid for large deformations. That is, tension, compression, and torsion experimental data for large deformation cannot be correlated by an effective stress-strain representation [2, 3]. The torsional effective stress-strain curve lies significantly below both the tensile and the compressive stress-strain curves at large strains. To simulate armor-antiarmor interaction accurately, it is necessary that the constitutive models in computer codes follow the response of the material at finite deformation more closely. These models should also be valid for nonmonotonic finite deformation loading situations.

Thin-wall tubular torsion testing is widely used to obtain the shear stress-shear strain response of materials for small strains. When these specimens are twisted to large shear strains, material elements in the gauge area of the specimen rotate by significant amounts. In spite of the ability to obtain large shear strains and rotations, this type of testing is not that widely used for the evaluation and the development of finite deformation plastic models.

It has been experimentally observed that when torsion tests are conducted with thin-wall tubular specimens either under fixed-end (no axial strain) or free-end (no axial stress) conditions, there will be an axial response: an axial stress in the fixed-end case and an axial strain in the free-end case [3, 4]. These axial effects can be explained by the evolution of texture; they can be predicted by polycrystal methodologies based on crystal plasticity [3-7]. Also phenomenological methods for small strains have been extended, with limited success, in trying to explain these experimentally observed axial responses [8-10]. Because the predicted axial response is extremely sensitive to the finite plasticity methods used in the predictive schemes, the axial measurement is a good tool for evaluating these models [6]. In spite of this, only few large strain experimental studies on thin-wall tubular specimens are available in the literature with axial measurements [3, 4, 7, 8, 11]. In addition, there is a reported study on solid specimens with axial measurements [5]. Because the stress varies along the radius, experiments on solid

specimens add another level of complexity to the evaluation of finite plasticity models; therefore, experiments with solid specimens are less attractive for model evaluations. All but one of the thin-wall specimen studies have been conducted with a monotonically increasing shear strain. To evaluate finite plasticity methods that are also applicable for a single reversal of loading after a large prestrain, experimental data are necessary for large deformation following changes in the path of straining. These experimental data are also important in studying plastic instabilities due to strain localization. Analyses of Pierce et al. [12] and Iwakuma and Nemat-Nasser [13] showed that the transient response during nonmonotonic loading and the corresponding changes in the instantaneous elastic-plastic moduli affect the plastic instabilities. The only reported study that measures the axial response following a change in the path of straining after a finite prestrain has been conducted by Lipkin and Lowe [11]. They have obtained axial and shear stress responses of 306L stainless steel for reverse loading after a finite prestrain of 1.6. In the evaluation of the polycrystal method, they used a portion of the results from the same test (shear stress response) to obtain the parameters of the crystal constitutive model. The gripping arrangement used in these tests produced a backlash, thus distorting both shear and axial stress transients just after change in the direction of loading.

The main objective of this work is to obtain experimental forward/reverse torsional data for larger strains for another material. It will then make it possible to fully evaluate large deformation constitutive methodologies, especially crystal plasticity methods. The stress-strain distortions observed by Lipkin and Lowe [11] due to the backlash in their experiments are eliminated with a different gripping arrangement of the specimen. In contrast to the work of Lipkin and Lowe [11], parameters of the crystal constitutive model are obtained from a different type of test (uniaxial compressive test conducted for large strain). None of the torsional tests results is used in the crystal plasticity analysis. Therefore, the procedure employed in this paper is a better method for evaluation of the large deformation polycrystal methods. Also, instead of using the more complex numerical integration scheme employed by Lipkin and Lowe [11], crystal plasticity simulations reported here are conducted with a relatively simpler integration scheme by Kalidindi et al. [7]. This scheme can be used with a microcomputer instead of a supercomputer and hence can be used by more researchers. This work provides an evaluation of the polycrystal method by Asaro and Needleman [14] with the new integration scheme.

This report presents the shear and axial stress responses of the experimental forward/reverse torsional study that was conducted under fixed-end (zero relative axial displacement) conditions. Thin-walled oxygen-free-high-conductivity (OFHC) copper specimens are monotonically strained for a maximum forward strain of 2.2 before reversing the strain to zero. OFHC copper was chosen as the material for the following reasons: 1) OFHC copper was previously studied

under monotonically increasing uniaxial compression as well as torsion loading conditions for large strains. Single-crystal model parameters are already available from this study [3]. 2) OFHC copper is a single-phase material, and its deformation can be simulated using existing crystal plasticity methods. 3) This material can be deformed to large shear strains before failure and therefore is suitable for large deformation studies. 4) Copper is used in shape charged jets and is of interest to the Army. Axial and shear stress responses for forward/reverse shear loading are also computed with a Taylor-type polycrystal methodology (Asaro and Needleman [14]) and compared with the experimental observations. Taylor predictions are obtained by a combined experimental and analytical procedure; single-crystal model parameters are obtained from uniaxial compression experiments, and then this model is used to obtain the fixed-end torsional test predictions.

2. Experimental Stress-Strain Behavior

2.1 Material.

Test specimens were machined from OFHC copper (99.99% copper). OFHC copper was received as bar stocks in the work-hardened condition. Torsion specimens were machined from this bar stock and were annealed after machining at 400° C in argon for 1 hr. This annealing heat treatment produced equiaxed grains of average diameter of 45 μm .

2.2 Experimental Procedure.

Specimen geometry of the torsion test specimen is given elsewhere [2]. This specimen is a modified Lindholm-type specimen that was used by White, Bronkhorst, and Anand [8] and Weerasooriya and Swanson [3]. The gauge portion of the torsion specimen is a thin-wall tube of 0.240 in. (6.096 mm) length and external and internal diameters of 0.810 in. (20.574 mm) and 0.750 in. (19.050 mm), respectively (0.030-in. wall thickness). The torsion tests were conducted using a tension-torsion hydraulic test machine. Specimens were attached to the test machine using a pair of hydraulic collet grips, thus eliminating any backlash similar to that observed by Lipkin and Lowe [11]. First, the specimen was twisted in a forward direction at a constant angular rate. Then the specimen was twisted in the reverse direction to the original position at the same angular rate. During both forward and reverse rotation, relative distance between the grips was kept constant to the extent of the ability of the test machine (within ± 0.0025 mm). The rate of twisting was chosen to give a nominal shear strain rate of 0.001 s^{-1} for these forward/reverse fixed-end torsion tests.

Experimental torque, axial load, and rotational information were converted to shear stress, axial stress, and shear strain by using the thin-wall assumption for the gauge area of the specimen. Shear stress was derived using the expression

$$\text{Shear stress} = \text{Torque} / (2\pi r_m^2 t), \quad (1)$$

where r_m is the mean radius of the gauge section and t is the wall thickness of the gauge area. The axial stress was obtained by

$$\text{Axial stress} = \text{Axial force} / (\pi(R^2 - r^2)), \quad (2)$$

where R is the outer radius and r is the inner radius. The engineering shear strain was given by the expression

$$\text{Shear strain} = (R\theta)/\text{Gauge length}, \quad (3)$$

where θ (in radians) is the relative rotation at the grips.

2.3 Torsion Test Results.

Typical shear and axial stress vs. engineering shear strain curves obtained from fixed-end torsion tests are given in Figure 1. As can be seen, the experimental shear stress increases with shear strain up to a strain of 2.2. When the direction reverses, shear stress elastically rapidly decreases and reaches a negative value. Figure 2 shows the magnitude of shear stress plotted as a function of the total magnitude of shear strain. Experimental results do show a small Bauschinger effect. The slope of shear stress vs. shear strain decreases (between A and B in Figure 2) and increases again and then approaches a steady rate (between B and C) with further straining in the reverse direction.

The axial stress is shown as a function of shear strain in Figure 3. Initially, the axial stress is compressive and reaches a peak value of about 23 MPa at an approximate shear strain of 1.2 as the shear strain is increased in the forward direction. When the shear strain reaches 2.2, the magnitude of compressive axial stress decreases to 5 MPa. Previous experiments [3] have shown that if the shear strain is increased further in the forward direction, the axial stress would become tensile.

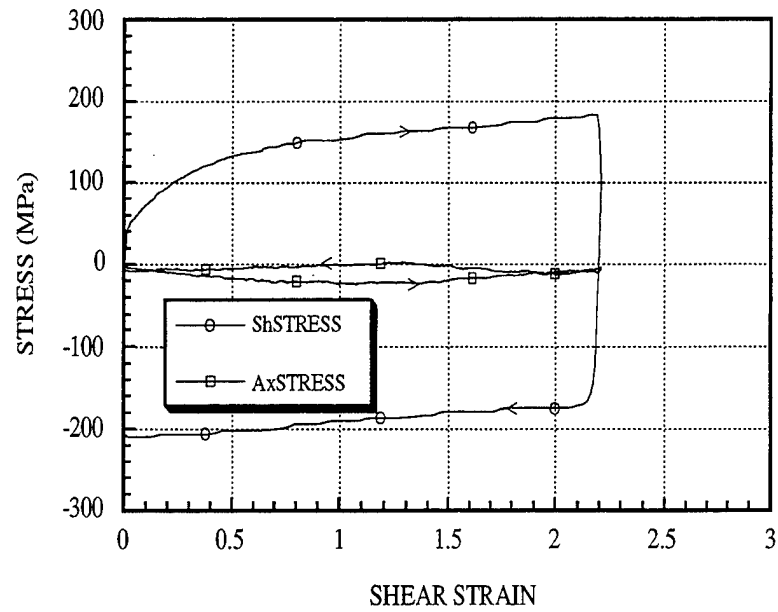


Figure 1. Experimental Shear and Axial Stresses Plotted as a Function of Shear Strain.

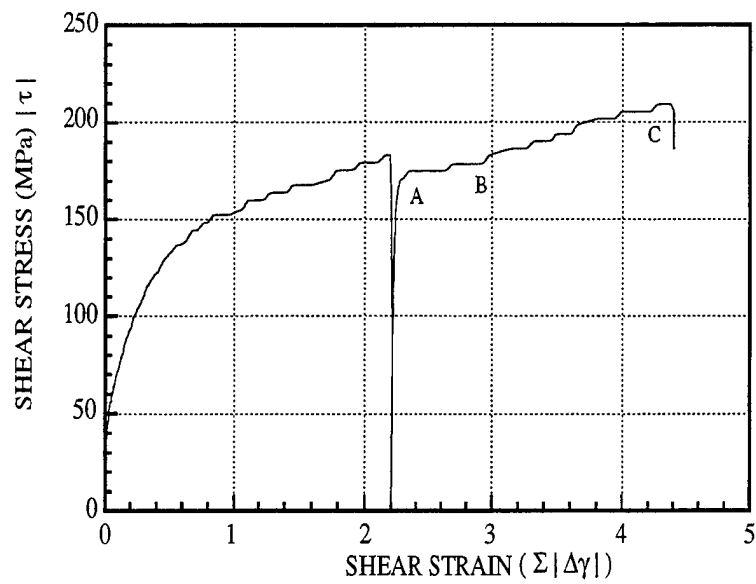


Figure 2. Magnitude of Experimental Shear Stresses Plotted as a Function of Total Shear Strain Showing a Small Bauschinger Effect.

When the strain is reversed, the magnitude of the axial compressive stress increases slightly before starting to decrease. As the strain is decreased further, the axial compressive stress decreases to zero. The axial stress then becomes tensile briefly before changing back to compression and starts to increase in magnitude again. This axial stress response is different from that observed by Lipkin and Lowe [11] for 304L stainless steel. For stainless steel, the axial compressive stress never reached a peak in the forward loading segment. Additional experiments are needed to fully explain these differences.

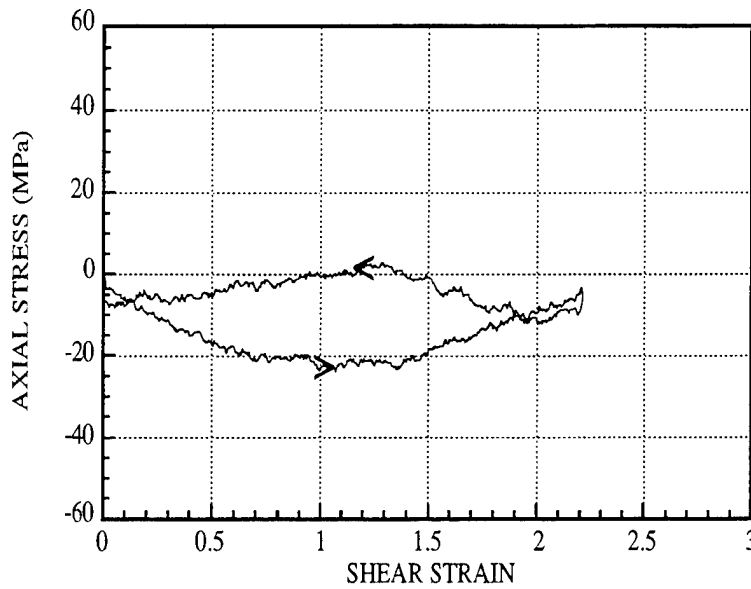


Figure 3. Experimental Axial Stress Plotted as a Function of Shear Strain.

3. Polycrystal (Taylor) Model Prediction

An overview of the Taylor-type rate-dependent polycrystal model of Asaro and Needleman is given in this section. We followed the formulation of the time integration of the polycrystal model as proposed by Kalidindi, Bronkhorst, and Anand [7]. The summary of their integration algorithm is also given in this section. With this formulation, the problem could be solved with PCs in view of the efficiency of the algorithm. The disadvantage of this formulation is that it can be applied easily only with the prescribed displacement boundary conditions. Mixed boundary condition problems can be solved by incorporating the polycrystal procedure in a finite element scheme.

3.1 Kinematics of the Single Crystal.

Let \mathbf{F} be the global deformation gradient of the polycrystalline material. With the Taylor assumption, the deformation gradient of each constituent crystal of the polycrystal will have the same deformation gradient \mathbf{F} . By multiplicative decomposition of the deformation gradient into elastic and plastic components, we obtain

$$\mathbf{F} = \mathbf{F}^e \mathbf{F}^p, \quad (1)$$

where \mathbf{F}^e is the elastic and \mathbf{F}^p is the plastic parts of the deformation gradient. Here \mathbf{F}^p is the deformation gradient due to plastic slip only ($\det \mathbf{F}^p = 1$); it represents an elastically unloaded intermediate relaxed configuration of a stress free state with the orientation of the crystal lattice coinciding with the crystal lattice in the reference configuration. The deformation gradient \mathbf{F}^e represents both rotation and elastic stretching of the crystal lattice ($\det \mathbf{F}^e > 1$). Then the velocity gradient \mathbf{L} is

$$\mathbf{L} = \dot{\mathbf{F}}\mathbf{F}^{-1} = \dot{\mathbf{F}}^e \mathbf{F}^{e-1} + \mathbf{F}^p \mathbf{L}_o^p \mathbf{F}^{e-1}, \quad (2)$$

where

$$\mathbf{L}_o^p = \dot{\mathbf{F}}^p \mathbf{F}^{p-1} \quad (3a)$$

or

$$\dot{\mathbf{F}}^p = \mathbf{L}_o^p \mathbf{F}^p. \quad (3b)$$

Here the notation $(\dot{})$ indicates the derivative with respect to time. Since \mathbf{L}_o^p is the plastic velocity gradient in the relaxed configuration, \mathbf{L}_o^p is given by

$$\mathbf{L}_o^p = \sum_{\alpha=1}^{12} \dot{\gamma}^\alpha \mathbf{S}_o^\alpha, \text{ where } \mathbf{S}_o^\alpha = \mathbf{s}_o^\alpha \otimes \mathbf{n}_o^\alpha, \quad (3c)$$

where \mathbf{s}_o^α and \mathbf{n}_o^α are orthonormal unit vectors representing slip directions and slip planes, respectively, for each slip system α in the reference configuration and the $\dot{\gamma}^\alpha$ is the plastic shearing rate in the α th slip system. For an fcc crystal, there are 12 slip systems derived from its four $\{111\}$ slip planes and three $\langle 110 \rangle$ slip directions from each slip plane. Consequently, in the α th slip system $(\mathbf{n}_o^\alpha, \mathbf{s}_o^\alpha)$, the unit vector \mathbf{n}_o^α represents a slip plane out of the four $\{111\}$ planes

and the unit vector \mathbf{s}_o^α represents a slip direction out of three corresponding $\langle 110 \rangle$ directions of the \mathbf{n}_o^α slip plane. From equation (2),

$$\mathbf{L}^p = \mathbf{D}^p + \mathbf{W}^p = \mathbf{F}^p \mathbf{L}_o^p \mathbf{F}^{e-1} = \sum_{\alpha=1}^{12} \dot{\gamma}^\alpha \mathbf{S}^\alpha, \text{ where } \mathbf{S}^\alpha = (\mathbf{F}^e \mathbf{s}_o^\alpha) \otimes (\mathbf{n}_o^\alpha \mathbf{F}^{e-1}), \quad (4a)$$

where \mathbf{D}^p and \mathbf{W}^p are plastic stretch and spin tensors, respectively, and are given by

$$\mathbf{D}^p = \sum_{\alpha=1}^{\alpha} \dot{\gamma}^\alpha \text{sym}\{\mathbf{S}^\alpha\} \text{ and } \mathbf{W}^p = \sum_{\alpha=1}^{\alpha} \dot{\gamma}^\alpha \text{asym}\{\mathbf{S}^\alpha\}. \quad (4b)$$

The rate of plastic stress power per unit reference volume is (see Anand [15])

$$\dot{\omega}^p = (\mathbf{C}^e \mathbf{T}^*): \mathbf{L}^p, \quad \text{with } \mathbf{C}^e = \mathbf{F}^{eT} \mathbf{F}^e \quad (5)$$

and

$$\mathbf{T}^* = \mathbf{F}^{e-1} \{(\det \mathbf{F}^e) \mathbf{T}\} \mathbf{F}^{e-T}. \quad (6)$$

The stress \mathbf{T} is the Cauchy stress of the crystal. The second Piola-Kirchhoff stress, \mathbf{T}^* , is the elastic work conjugate of the Lagrangean elastic strain measure

$$\mathbf{E}^e = (1/2) \{ \mathbf{C}^e - \mathbf{I} \}, \quad \text{with } \mathbf{C}^e = \mathbf{F}^{eT} \mathbf{F}^e \quad (7)$$

But the plastic stress power per unit volume is

$$\dot{\omega}^p = \sum_{\alpha=1}^{12} \tau^\alpha \dot{\gamma}^\alpha, \quad (8)$$

where τ^α is the resolved shear stress in the α th slip system. Therefore, from equations (5) and (8), resolved shear stress

$$\tau^\alpha = (\mathbf{C}^e \mathbf{T}^*): \mathbf{S}_o^\alpha. \quad (9)$$

3.2 Crystal Plasticity Constitutive Model.

Single-crystal constitutive behavior relating the resolved shear stress, τ^α , and resolved shear strain rate, $\dot{\gamma}^\alpha$, is given by the viscoplastic rate power law

$$\dot{\gamma}^\alpha = \dot{\gamma}_0 \left| \frac{\tau^\alpha}{s^\alpha} \right|^{1/m} \text{sign}(\tau^\alpha). \quad (10)$$

where $\dot{\gamma}_0$ is the reference shear strain rate, s^α is the resistance of the slip system α (defined by the slip plane and the slip direction - total of 12 slip systems for fcc copper crystal), and m is the strain rate sensitivity parameter (assumed to be the same for all slip systems). Also, s^α can be considered as the slip resistance of the slip system α at the reference shearing rate, $\dot{\gamma}_0$.

The slip resistance s^α is evolved according to

$$s^\alpha = \sum_{\beta=1}^{12} h^{\alpha\beta} |\dot{\gamma}^\beta|, \quad (11)$$

where $h^{\alpha\beta}$ is the instantaneous hardening modulus of the slip system α due to a shearing on the slip system β . The form of the hardening moduli is given by

$$h^{\alpha\beta} = h(s^\beta) q^{\alpha\beta} \quad (\text{no sum of } \beta), \quad (12)$$

where $q^{\alpha\beta}$ is a 12 by 12 matrix describing the relationship between self- and latent-hardening behavior of the crystal slip systems. The ratio of latent-hardening to self-hardening is assumed to be unity for coplanar and a value of 1.4 for noncoplanar systems. The slip-hardening modulus, $h(s)$, is assumed to be given by

$$h(s) = h_0 \left(1 - \frac{s}{s_s} \right)^a, \quad (13)$$

where constants h_0 , s_s , and a are assumed to be the same for all slip systems. Here, s_s represents the saturated slip resistance and h_0 is a measure of the initial hardening modulus of the single slip system. From this assumed slip-hardening behavior, after integrating equation (13)

$$\left(|\gamma| = \int_0^\gamma d\gamma = \int_{s_0}^s \frac{ds}{h(s)} \right),$$

$$|\gamma| = \frac{s_s}{(1+a)} \left[\left(1 - \frac{s}{s_s}\right)^{-(a+1)} - \left(1 - \frac{s_0}{s_s}\right)^{-(a+1)} \right] \quad (14)$$

for $a \neq -1$, where s_0 is the initial slip resistance and the $|\gamma|$ is the absolute value of shear strain. Here, the Bauschinger effect is assumed to be negligible.

From finite elasticity, the reduced constitutive equation for an elastic material in a grain can be written in the form

$$\mathbf{T}^* = \mathcal{L}[\mathbf{E}^e], \quad (15)$$

where \mathcal{L} is the fourth-order elastic tensor. Assuming all the grains are of equal volume, with the Taylor assumption that the local deformation gradient of each grain is the same as the global deformation gradient, then the volume average Cauchy stress \mathbf{T}^G is

$$\mathbf{T}^G = \frac{1}{N} \sum_{k=1}^N \mathbf{T}^k, \quad (16)$$

where \mathbf{T}^k is the Cauchy stress of each grain and N is the number of grains. The volume average stress \mathbf{T}^G is the global stress response of the polycrystal (Asaro and Needleman [14]).

In the reformulation of the Asaro-Needleman polycrystal method with their efficient time-integration scheme, Kalidindi, Bronkhorst, and Anand [7] have assumed the following approximations:

For small isotropic elastic stretches:

$$\mathcal{L} = 2\mu \mathbf{I} + \left(\kappa - \frac{2\mu}{3}\right) \mathbf{1} \otimes \mathbf{1} \quad (17)$$

and

$$\tau^\alpha \approx \mathbf{T}^* : \mathbf{S}^\alpha. \quad (18)$$

3.3 Numerical Procedure for Model Predictions.

In the simulation of the experiments reported in this report, the time-integration procedure proposed by Kalidindi et al. was used to integrate the aforementioned polycrystal methodology. This formulation of the time-integration procedure is summarized in this section.

The problem of integrating this polycrystal model can be summarized as follows. Let λ be the time Δt after the current time t . Then the problem is to find the list $\{ \mathbf{F}^p(\lambda), \mathbf{s}^\alpha(\lambda), \mathbf{T}(\lambda) \}$ for each grain at time λ when the current state $\{ \mathbf{F}^p(t), \mathbf{s}^\alpha(t), \mathbf{T}(t) \}$ of all the grains and the global deformation gradients at t and λ are given. Once the stress at each grain is known, global stress behavior at λ can be calculated from equation (16). Following equation (4a), the new texture at the time λ for each crystal can be computed.

$$\mathbf{s}_\lambda^\alpha = \mathbf{F}^c(\lambda) \mathbf{s}_0^\alpha \quad (19)$$

and

$$\mathbf{n}_\lambda^\alpha = \mathbf{F}^{c-T}(\lambda) \mathbf{n}_0^\alpha, \quad (20)$$

where $(\mathbf{s}_\lambda^\alpha, \mathbf{n}_\lambda^\alpha)$ is the slip system in the deformed configuration. Since the slip systems in the undeformed configuration $(\mathbf{s}_0^\alpha, \mathbf{n}_0^\alpha)$ are orthonormal, the slip systems in the deformed configuration are also orthonormal. If $\mathbf{F}^c(\lambda)$ is found, then the slip system in the deformed configuration for each crystal at the time λ can be computed, and hence the pole figure can be constructed for the deformed polycrystal.

The starting point for the formulation of the time integration procedure is the result obtained by Weber and Anand [16] in the implicit time-integration of the evolution equation for $\dot{\mathbf{F}}^p$ given in equation (3b):

$$\mathbf{F}^p(\lambda) = \exp\{\Delta t \mathbf{L}^p(\lambda)\} \mathbf{F}^p(t). \quad (21)$$

By neglecting terms of higher order than $\Delta\gamma^\alpha$ for small $\Delta\gamma^\alpha$ and using equation (3c),

$$\mathbf{F}^p(\lambda) = \{\mathbf{I} + \sum_{\alpha=1}^{12} \Delta\gamma^\alpha \mathbf{S}_0^\alpha\} \mathbf{F}^p(t) \quad (22a)$$

or

$$\mathbf{F}^{p-1}(\lambda) = \mathbf{F}^{p-1}(t) \{\mathbf{I} - \sum_{\alpha=1}^{12} \Delta\gamma^\alpha \mathbf{S}_0^\alpha\}, \quad (22b)$$

where

$$\Delta\gamma^\alpha = \dot{\gamma}^\alpha(\lambda) \Delta t. \quad (23)$$

From equations (23), (18), and (10), $\Delta\gamma^\alpha$ is given by

$$\Delta\gamma^\alpha = \dot{\gamma}_0 \Delta t \left| \frac{\mathbf{T}^* : \mathbf{S}^\alpha}{s^\alpha} \right|^{1/m} \text{sign}(\mathbf{T}^* : \mathbf{S}^\alpha), \quad (24)$$

Substituting equations (7) and (1) in the elastic constitutive equation (15), the following equations are obtained (see Kalidindi et al. [7] for details):

$$\mathbf{T}^*(\lambda) = \mathbf{T}^{*tr} - \sum_{\alpha=1}^{12} \Delta\gamma^\alpha \mathbf{C}^\alpha, \quad (25)$$

and

$$s^\alpha(\lambda) = s^\alpha(t) + \sum_{\beta=1}^{12} h^{\alpha\beta} |\Delta\gamma^\beta|, \quad (26)$$

where

$$\mathbf{T}^{*tr} = \mu \mathbf{A} + \frac{3\kappa - 2\mu}{6} (\text{tr} \mathbf{A}) \mathbf{1} - \frac{3\kappa}{2} \mathbf{1}, \quad (27)$$

$$\mathbf{A} = \mathbf{F}^{p-T}(t) \mathbf{F}^T(\lambda) \mathbf{F}(\lambda) \mathbf{F}^{p-T}(t), \quad (28)$$

$$\mathbf{C}^\alpha = \mu \mathbf{B}^\alpha + \frac{3\kappa - 2\mu}{6} (\text{tr} \mathbf{B}^\alpha) \mathbf{1}, \quad (29)$$

and

$$\mathbf{B}^\alpha = \mathbf{A} \mathbf{S}_0^\alpha + \mathbf{S}_0^{\alpha T} \mathbf{A}. \quad (30)$$

Equations (25) and (26) are 2 sets of nonlinear simultaneous equations ($\mathbf{T}^*(\lambda)$ with 6 unknowns and $s^\alpha(\lambda)$ with 12 unknowns) and can be solved using a modified Newton-Raphson-type algorithm (see Kalidindi and coworkers [7] for the details of the algorithm). Once $\mathbf{T}^*(\lambda)$ and $s^\alpha(\lambda)$ are known, $\mathbf{F}^p(\lambda)$ is obtained using equation (22a) and $\mathbf{F}^e(\lambda)$ is obtained from equation (1). The new texture at time τ can be found by the polar decomposition of $\mathbf{F}^e(\lambda)$ into its elastic lattice rotation component [$\mathbf{R}^e(\lambda)$] and elastic stretching component and by using the equations (19) and (20) to obtain

$$\mathbf{s}_\lambda^\alpha = \mathbf{R}^e(\lambda) \mathbf{s}_0^\alpha \quad (31)$$

and

$$\mathbf{n}_\lambda^\alpha = \mathbf{R}^{e-T}(\lambda) \mathbf{n}_0^\alpha, \quad (32)$$

where $\mathbf{s}_\lambda^\alpha$ (slip direction) and $\mathbf{n}_\lambda^\alpha$ (slip plane) are unit vectors representing the slip system α at time λ .

A computer program based on the aforementioned algorithm is given elsewhere [3].

3.4 Model Predictions.

The computer program by Weerasooriya and Swanson [3] was modified to include forward/reverse loading. This revised program was used to obtain the polycrystal model predictions of the forward/reverse loading of the fixed-end torsion (simple shear) tests. Single-crystal model parameters obtained earlier from the uniaxial compressive test data [3] were employed in the simulations. The values of these parameters are strain rate sensitivity, $m = 0.012$; latent hardening, $q = 1.4$; initial hardening modulus, $h_0 = 700$ MPa; initial slip resistance, $s_0 = 16$ MPa; saturated slip resistance, $s_s = 155$ MPa; and the exponent in the hardening modulus, $a = 3.8$. The material elements are assumed to follow a simple shear motion, which is given by

$$\mathbf{x} = (X_1 + \dot{\gamma} t X_2) \mathbf{e}_1 + X_2 \mathbf{e}_2 + X_3 \mathbf{e}_3, \quad (33)$$

where $\dot{\gamma}$ is the engineering shear strain rate, $\mathbf{X} \{X_1, X_2, X_3\}$ and \mathbf{x} are the original and current positions of a material element, respectively, and $\mathbf{e}_i \{i = 1, 2, 3\}$ are orthonormal base vectors of a global rectangular Cartesian coordinate system. Here, \mathbf{e}_1 is the shear direction, \mathbf{e}_2 is the axial direction, and \mathbf{e}_3 is the radial direction of the specimen.

Computations were conducted using a PC. The initial crystallographic texture was assumed to be isotropic (the grains were randomly oriented); the initial distribution of the crystals were taken from Molinari et al. [17] and was given as 300 sets of Euler angles. Each set of Euler angles would rotate the axes ($\langle 100 \rangle$) of the corresponding crystal to coincide with the global fixed rectangular Cartesian axes. The Schmid tensor, \mathbf{S}_0^α , was computed with respect to the global coordinate system for each crystal by

$$\mathbf{S}_o^\alpha = \mathbf{Q} \mathbf{S}_c^\alpha \mathbf{Q}^T, \quad (34)$$

where \mathbf{S}_c^α is defined with respect to an orthonormal basis associated with the crystal lattice $\langle 100 \rangle$ directions. Twelve slip systems that define \mathbf{S}_c^α for fcc crystal are given in Table 1.

Table 1. Twelve Slip Systems for fcc Crystal

slip system α	slip plane \mathbf{n}^α	slip direction \mathbf{s}^α
1	$(1\ 1\ 1)/\sqrt{3}$	$[-1\ 1\ 0]/\sqrt{2}$
2	$(1\ 1\ 1)/\sqrt{3}$	$[-1\ 0\ 1]/\sqrt{2}$
3	$(1\ 1\ 1)/\sqrt{3}$	$[0\ -1\ 1]/\sqrt{2}$
4	$(-1\ 1\ 1)/\sqrt{3}$	$[1\ 1\ 0]/\sqrt{2}$
5	$(-1\ 1\ 1)/\sqrt{3}$	$[1\ 0\ 1]/\sqrt{2}$
6	$(-1\ 1\ 1)/\sqrt{3}$	$[0\ -1\ 1]/\sqrt{2}$
7	$(1\ -1\ 1)/\sqrt{3}$	$[1\ 1\ 0]/\sqrt{2}$
8	$(1\ -1\ 1)/\sqrt{3}$	$[0\ 1\ 1]/\sqrt{2}$
9	$(1\ -1\ 1)/\sqrt{3}$	$[1\ 0\ -1]/\sqrt{2}$
10	$(1\ 1\ -1)/\sqrt{3}$	$[0\ 1\ 1]/\sqrt{2}$
11	$(1\ 1\ -1)/\sqrt{3}$	$[1\ 0\ 1]/\sqrt{2}$
12	$(1\ 1\ -1)/\sqrt{3}$	$[1\ -1\ 0]/\sqrt{2}$

The orthogonal matrix \mathbf{Q} , which rotates the crystal basis to coincide with the global fixed basis, is given by

$$Q = \begin{bmatrix} \cos \phi \sin \theta & \sin \phi \cos \omega & \sin \omega \sin \theta \\ -\sin \phi \sin \omega \cos \theta & +\cos \phi \sin \omega \cos \theta & \\ -\cos \phi \sin \omega & -\sin \phi \sin \omega & \cos \omega \sin \theta \\ -\sin \phi \sin \omega \cos \theta & \cos \phi \cos \omega \cos \theta & \\ \sin \phi \sin \theta & -\cos \phi \sin \theta & \cos \theta \end{bmatrix}, \quad (35)$$

where $\{0 \leq \phi \leq 2\pi, 0 \leq \theta \leq \pi, 0 \leq \omega \leq 2\pi\}$ are the three Euler angles that represent this transformation. Our previous work showed that there was no appreciable difference in the results whether 300 or 100 crystals were used in simulations. Therefore, simulations were conducted with a subset of 100 crystals. The initial random distribution of these 100 crystals are given in Figure 4 as equal area projection $\{111\}$ pole figures.

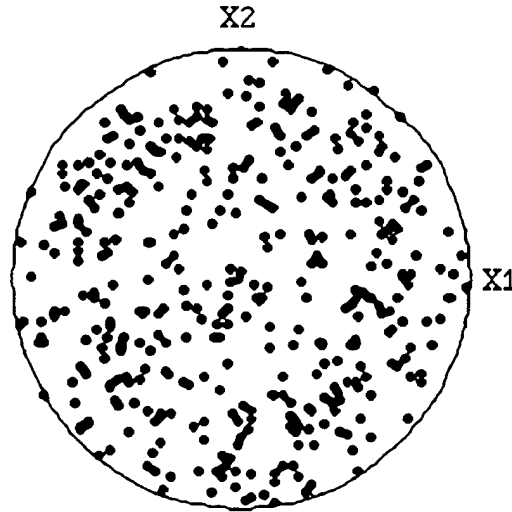


Figure 4. $\{111\}$ Equal-Area Projection Pole Figures of Initial Randomly Oriented 100 Crystals.

Figure 5 shows the shear (T12), axial (T22), and hoop (T11) stresses plotted as a function of shear strain from the polycrystal simulation. Predicted shear stress increases with increasing shear strain until the shear strain is reversed. After the direction of the shear strain is reversed, the shear stress rapidly (elastically) unloads to a negative value. When the magnitude of the shear stress reaches the maximum stress at the end of the forward loading, the work-hardening rate decreases and then starts to increase again. This work-hardening behavior is identical to that observed from experiments and is discussed earlier.

Axial and hoop stresses shown in Figure 5 are opposite in sign for a given strain. That is, when the axial stress is compressive, the hoop stress is tensile and vice versa. As the shear strain is increased in the forward direction, initially the axial stress is compressive. It reaches a compressive peak, and then the magnitude of the stress starts to decrease. When the loading is reversed, the axial stress rapidly decreases to zero and then becomes tensile. As the shear strain is reduced to zero, tensile axial stress reaches a tensile peak and decreases to a value close to zero.

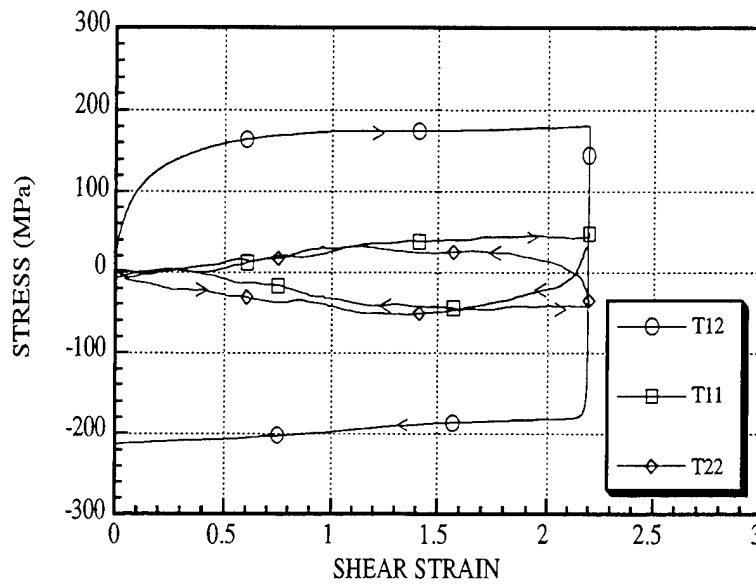


Figure 5. Predicted Shear, Axial, and Hoop Stresses as a Function of Shear Strain.

4. Comparison of Experimental Results With Polycrystal Model Predictions

Figure 6 compares the predicted and experimental shear stresses as a function of the shear strain. Figure 7 shows both the experimental and simulated magnitudes of shear stress plotted as a function of the total magnitude of shear strain. Because, in simulation, the single slip hardening behavior [see equation (14)] was assumed to have no Bauschinger effect, the prediction does not show any either. During initial forward loading, up to a shear strain of 1.5, shear stress predicted by the polycrystal plasticity method is higher than the experimental stress at most by 31 MPa (initial higher work-hardening rate in the prediction). However, beyond this shear strain, the model generated shear stress agrees with the experimental data extremely well (difference is at most 8 MPa).

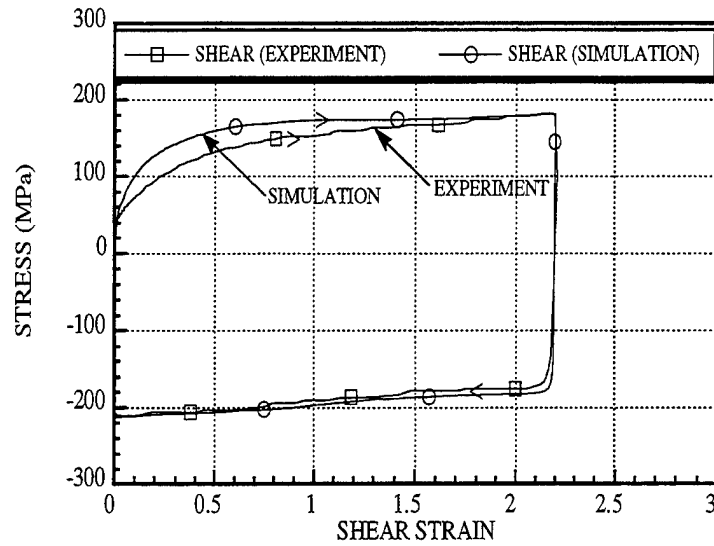


Figure 6. Comparison of Experimental and Predicted Shear Stresses as a Function of Shear Strain.

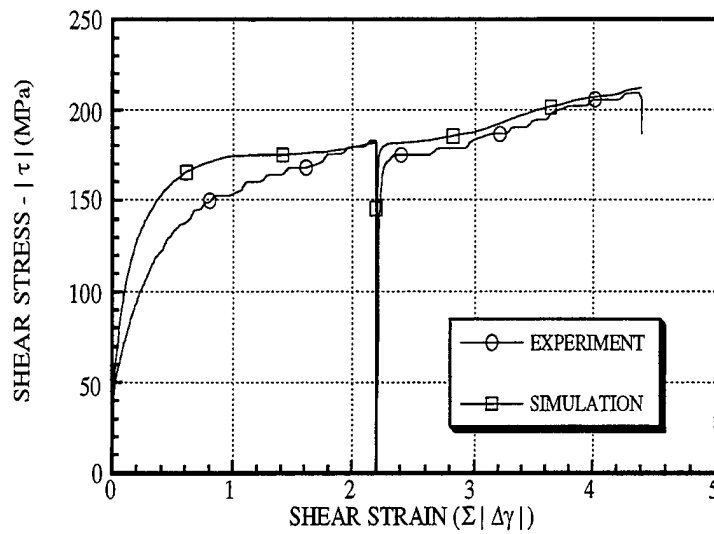


Figure 7. Magnitude of Experimental and Predicted Shear Stresses Plotted as a Function of Total Shear Strain. (A Small Bauschinger Effect Can Be Clearly Seen.)

Figure 8 compares the predicted and experimental axial stress-shear strain responses. The overall trend (loop)—initially compressive with a peak and then tensile with a peak—of both experimental and predicted axial stress responses is similar for most of the forward/reverse loading. In the forward loading segment, both experimental and predicted axial stresses are compressive; however, the magnitude of the prediction is larger than that from the experiments. Both experimental and predicted axial stresses reach a compressive peak, approximately at the same values of shear strain. When the shear strain is reversed, predicted compressive axial stress decreases rapidly; in contrast, the experimental compressive axial stress increases before it starts to decrease. Beyond this point, both predicted and experimental axial stresses reach tensile peaks and then decrease back to a small compressive residual stress as the specimen is twisted back to its original configuration (shear strain of zero). Shear strain values at these peaks during reverse loading are also approximately equal. Although the prediction shows a tensile stress during most of the reverse loading, experiments show a tensile stress only for a small section of the reverse loading segment. Even though the overall trends of both the predicted and experimental axial responses are similar, in general, the model overpredicts the magnitude of the experimental axial stress.

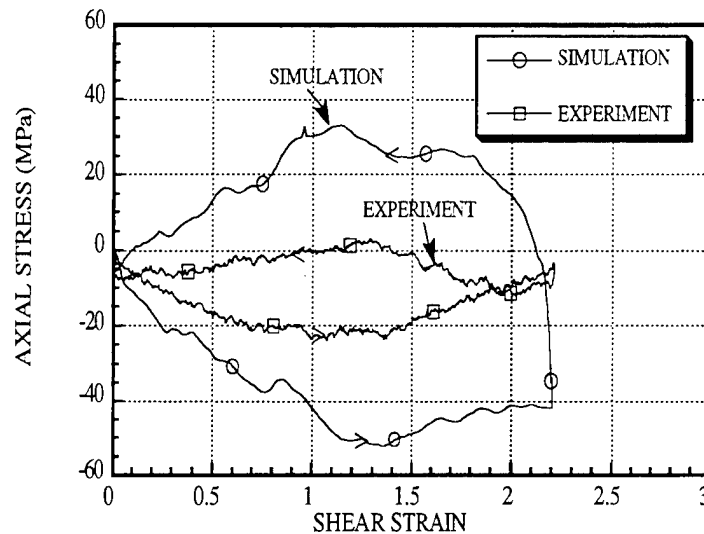


Figure 8. Experimental and Predicted Axial Stresses Plotted as a Function of Shear Strain.

The model simulation ideally assumes zero axial strain. In the fixed-end torsion experiments conducted by Weerasooriya and Swanson [3] and Lipkin and Lowe [11], they have shown that it is not possible to completely eliminate the axial strain in the gauge area. Appreciably large

combined compliance of the specimen outside the gauge area and the test machine is the reason for this axial strain. Simulation by Lowe and Lipkin [18] showed that the relaxation of the assumed zero axial strain constraint reduced the magnitude of the predicted axial stress.

The observed differences in the predicted and experimental axial stress transients just after the change in the direction of loading may also be due to the large combined compliance of the specimen (outside the gauge area) and the test machine. This combined compliance could be a nonlinear function of the displacement due to some plastic deformation at the tapered shoulder of the specimen. During loading, rate of rotation at the rotation measuring device of the test machine is kept constant. If the compliance between the rotation measuring device and the gauge area is appreciable, the relative rotation at the ends of the gauge area does not follow the applied rotation to the test machine. Especially when the loading is reversed, relative rotation at the gauge area could follow a complex response that could even include changes in the direction of loading. Therefore, the experimental axial stress transient response after the load reversal is not reliable.

Based on the results, the following recommendations are suggested for future work. In the experiments, to eliminate any axial strain in the gauge area, torsion tests can be conducted with real-time measurement and control of the axial strain. Controlling axial strain in the gauge area requires complex new extensometry that should fit into the short gauge section with large rotational displacements. The other possibility is to measure the average axial strains in the gauge area using an optical method, while the experiments are being conducted with the relative axial displacement between the grips held at zero. In this case, during simulation, the measured axial strain can be used as an input boundary condition.

The Taylor method assumes a uniform deformation gradient tensor for each grain that is identical to the applied global deformation gradient. Though this assumption satisfies the compatibility between grains, it violates the equilibrium condition. If the simulation is conducted using a finite element code with the polycrystal procedure implemented in it, we could have obtained a better agreement between simulated and experimental stress-strain data. In this case, at least between the elements, the equilibrium condition is satisfied. Such a procedure is recently suggested by Kalidindi using the ABAQUS finite element code [19]. He has shown that with this procedure, the prediction closely resembled the experimental results.

5. Summary and Conclusions

Experimental data for a thin-wall tubular OFHC copper specimen subjected to reverse torsional loading after a large prestrain in the forward direction were presented in this report. The tests were conducted at a shear strain rate of 0.001 s^{-1} under fixed-end conditions (zero axial displacement). Experimental results were presented as axial stress vs. shear strain plots. Data also include the shear stress in the thin tubular specimen. The experimental shear and axial stress responses are compared with the Taylor-type polycrystal model predictions. For the simulation, parameters for single-crystal constitutive behavior were obtained from large deformation uniaxial compression experiments.

In general, the predicted shear behavior agreed with the experimental measurements; a difference of at most 31 MPa was observed between the measured and the predicted shear stresses in the forward loading up to the shear strain of 1.5. For the rest of the forward and reverse straining, the predicted followed the experimental results reasonably well.

Although the simulated axial stress was higher than the experimental axial stress, the predicted overall response was similar for most of the shear loading; both predicted and experimental axial stress responses reached a compressive peak during the forward straining and a tensile peak during the reverse straining, at approximately same values of shear strains. Due to the inherent complexities in the experimentation (inability in holding axial strain in the gauge area at exactly zero), the experimental axial transient response just after the change of the direction of loading was different from the corresponding predicted stress transient.

In conclusion, the Taylor-type polycrystal method, with the assumed simple shear boundary condition, predicts the shear stress response reasonably well. The model-calculated axial stress response for most of the forward and reverse loading matched the salient features of the data.

Axial compliance of the load train and the specimen outside the gauge area affects the experimental axial stress response. Due to the inherent difficulties in conducting ideal simple shear experiments, a reformulated Taylor procedure with the measured axial displacement boundary conditions can be a better predictive method of the experimental results.

6. References

1. Batra, R. C., and T. Gobinath. "Steady State Axisymmetric Deformations of a Thermoviscoplastic Rod Penetrating a Thick Thermoviscoplastic Target." *International Journal of Impact Engineering*, vol. 8, p. 99, 1989.
2. Semiatin, S. L., G. D. Lahoti, and J. J. Jonas. *Mechanical Testing - Metals Handbook*. Ninth Edition, vol. 8, p. 164, 1985.
3. Weerasooriya, T., and R. Swanson. "Experimental Evaluation of the Taylor-Type Polycrystal Model for the Finite Deformation of an FCC Metal (OFHC Copper)." MTL TR 91-20, U.S. Army Materials Technology Laboratory, Watertown, MA, 1991.
4. Lipkin, J., M. L. Chiesa, and D. J. Bamman. "Thermal Softening of 304L Stainless Steel: Experimental Results and Numerical Simulations." *Proceedings of IMPACT'87*, Bremen, FRG, 1987.
5. Montheillet, F. M., M. Cohen, and J. J. Jonas. "Axial Stresses and Texture Development During the Torsion Testing of Al, Cu and α -Fe." *Acta Metallurgica*, vol. 32, pp. 2077-2089, 1984.
6. Harren, S., T. C. Lowe, R. J. Asaro, and A. Needleman. "Analysis of Large-strain Shear in Rate-dependent Face-centered Cubic Polycrystals: Correlation of Micro- and Macromechanics." *Philosophical Transaction of Royal Society*, vol. 328, pp. 443-500, 1989.
7. Kalidindi, S. R., C. A. Bronkhorst, and L. Anand. "Crystallographic Texture Evolution in Bulk Deformation Processing of fcc Metals." *Journal of the Mechanics and Physics of Solids*, vol. 40, pp. 537-569, 1992.
8. White, C. S., C. A. Bronkhorst, and L. Anand. "An Improved Isotropic-Kinematic Hardening Model for Moderate Deformation Metal Plasticity." *Mechanics of Materials*, vol. 10, pp. 127-147, 1990.
9. Bamman, D. J. "An Internal Variable Model of Viscoplasticity." *International Journal Engineering Science*, vol. 22, pp. 1041-1053, 1984.
10. Aifantis, E. C. "The Physics of Plastic Deformation." *International Journal of Plasticity*, vol. 3, pp. 211-247, 1987.
11. Lipkin, J., and T. C. Lowe. "Axial Effects During Reversed Torsional Deformation." *Proceeding of Plasticity' 89: The Second International Symposium on Plasticity and Its Current Applications*, Kahn and Tokuda (editors), Tsu, Mie Prefecture, Japan, 1989.
12. Peirce, D., R. J. Asaro, and A. Needleman. "An Analysis of Nonuniform and Localized Deformation in Ductile Single Crystals." *Acta Metallurgica*, vol. 31, pp. 1951-1976, 1983.

13. Iwakuma, T., and S. Nemat-Nasser. *Proceedings of Royal Society London A*, vol. 394, pp. 87–119, 1984.
14. Asaro, R. J., and A. Needleman. “Texture Development and Strain Hardening in Rate Dependent Polycrystals.” *Acta Metallurgica*, vol. 33, pp. 923–953, 1985.
15. Anand, L. “Constitutive Equations for Hot-Working of Metals.” *International Journal of Plasticity*, vol. 1, pp. 213–231, 1985.
16. Weber, G., and L. Anand. “Finite Deformation Constitutive Equations and a Time Integration Procedure for Isotropic, Hyperelastic-Viscoplastic Solids.” *Computer Methods Applied Mechanical Engineering*, vol. 79, pp. 173–202, 1990.
17. Molinari, A., G. R. Canova, and S. A. Ahzi. “Self-Consistent Approach of the Large Deformation Polycrystal Viscoplasticity.” *Acta Metallurgica*, vol. 35, pp. 2983–2994, 1987.
18. Lowe, T. C., and J. Lipkin. “Analysis of Axial Deformation Response During Reverse Shear.” SAND90-8417, Sandia National Laboratory, Albuquerque, NM, 1990.
19. Kalidindi, S. R., “Polycrystal Plasticity: Constitutive Modeling and Deformation Processing.” Ph. D. Thesis, MIT, Cambridge, MA, 1992.

NO. OF
COPIES ORGANIZATION

2 DEFENSE TECHNICAL
INFORMATION CENTER
DTIC DDA
8725 JOHN J KINGMAN RD
STE 0944
FT BELVOIR VA 22060-6218

1 HQDA
DAMO FDQ
DENNIS SCHMIDT
400 ARMY PENTAGON
WASHINGTON DC 20310-0460

1 OSD
OUSD(A&T)/ODDDR&E(R)
R J TREW
THE PENTAGON
WASHINGTON DC 20301-7100

1 DPTY CG FOR RDE HQ
US ARMY MATCOM
AMCRD
MG BEAUCHAMP
5001 EISENHOWER AVE
ALEXANDRIA VA 22333-0001

1 INST FOR ADVNCD TCHNLGY
THE UNIV OF TEXAS AT AUSTIN
PO BOX 202797
AUSTIN TX 78720-2797

1 DARPA
B KASPAR
3701 N FAIRFAX DR
ARLINGTON VA 22203-1714

1 NAVAL SURFACE WARFARE CTR
CODE B07 J PENNELLA
17320 DAHLGREN RD
BLDG 1470 RM 1101
DAHLGREN VA 22448-5100

1 US MILITARY ACADEMY
MATH SCI CTR OF EXCELLENCE
DEPT OF MATHEMATICAL SCI
MAJ M D PHILLIPS
THAYER HALL
WEST POINT NY 10996-1786

NO. OF
COPIES ORGANIZATION

1 DIRECTOR
US ARMY RESEARCH LAB
AMSRL D
J W LYONS
2800 POWDER MILL RD
ADELPHI MD 20783-1145

1 DIRECTOR
US ARMY RESEARCH LAB
AMSRL DD
J J ROCCHIO
2800 POWDER MILL RD
ADELPHI MD 20783-1145

1 DIRECTOR
US ARMY RESEARCH LAB
AMSRL CS AL TA
2800 POWDER MILL RD
ADELPHI MD 20783-1145

3 DIRECTOR
US ARMY RESEARCH LAB
AMSRL CI LL
2800 POWDER MILL RD
ADELPHI MD 20783-1145

ABERDEEN PROVING GROUND

4 DIR USARL
AMSRL CI LP (305)

<u>NO. OF COPIES</u>	<u>ORGANIZATION</u>	<u>NO. OF COPIES</u>	<u>ORGANIZATION</u>
1	COMMANDER US ARMY ARDEC G FLEMING PICATINNY ARSENAL NJ 07806-5000	1	PENN STATE UNIVERSITY COLLEGE OF ENGINEERING R GERMAN UNIVERSITY PARK PA 16802-6809
2	COMMANDER US ARMY ARDEC AMSTA AR FSA E E BAKER D KAPOOR PICATINNY ARSENAL NJ 07806-5000	1	BROWN UNIVERSITY DIV OF ENGINEERING R CLIFTON PROVIDENCE RI 02912
2	SOUTHWEST RSRCH INSTITUTE C ANDERSON J LANKFORD PO DRAWER 28510 SAN ANTONIO TX 78228-0510	1	UC SAN DIEGO DEPT APPL MECH AND ENG SVCS R011 S NEMAT-NASSER LA JOLLA CA 92093-0411
1	DIRECTOR LOS ALAMOS NATIONAL LAB MS B296 G T GRAY PO BOX 1663 LOS ALAMOS NM 87545	1	CALTECH G RAVICHANDRAN MS 105-50 1201 E CALIFORNIA BLVD PASADENA CA 91125
1	AIR FORCE WRIGHT LAB TECH LIB J FOSTER ARMAMENT DIVISION 101 EGLIN AVE STE 239 EGLIN AFB FL 32542	1	INST OF ADVANCE TECH UNIV OF TX AUSTIN S J BLESS 4030 2 W BRAKER LN AUSTIN TX 78759
1	LOS ALAMOS NATIONAL LAB D RABERN GROUP MEE 13 MSJ576 LOS ALAMOS NM 87545	1	COMMANDER US ARMY RSRCH OFFC K IYER PO BOX 12211 RESEARCH TRIANGLE PARK NC 27709-2211
1	LOS ALAMOS NATIONAL LAB TECH LIB PO BOX 1663 LOS ALAMOS NM 87545	1	VIRGINIA POLYTECHNIC INST COLLEGE OF ENGR R BATRA BLACKSBURG VA 24061-0219
1	JOHNS HOPKINS UNIVERSITY DEPT MECH ENGINEERING K RAMESH CHARLES AND 33 ST BALTIMORE MD 21218	1	GIAT INDUSTRIES DIV. SYS. D'ARMES MUNITION H COUQUE 7 ROUTE DE GUERRY 18000 BOURGES, FRANCE
		1	DIR LLNL D LASILA L170 LIVERMORE CA 94550

<u>NO. OF COPIES</u>	<u>ORGANIZATION</u>	<u>NO. OF COPIES</u>	<u>ORGANIZATION</u>
	<u>ABERDEEN PROVING GROUND</u>		AMSRL WM MB
68	DIR USARL		B BURNS
	AMSRL WM TD		C HOPPEL
	S CHOU		G GAZONAS
	A M DIETRICH		
	D DANDEKAR		
	A RAJENDRAN		
	T HADUCH		
	S SCHOENFELD		
	K FRANK		
	F. GREGORY		
	M RAFTENBERG		
	J WALTERS		
	T WRIGHT		
	P KINGMAN		
	S SEGLETES		
	T WEERASOORIYA (25 CPS)		
	AMSRL WM TC		
	W DEROSSET		
	T BJERKE		
	E KENNEDY		
	R MUDD		
	W WALTERS		
	L MAGNESS		
	R COATES		
	B SORENSON		
	D SCHEFFLER		
	K KIMSEY		
	AMSRL WM TA		
	W GILLICH		
	W BRUCHEY		
	M BURKINS		
	E RAPACKI		
	N RUPERT		
	J RUNYEON		
	W A GOOCH		
	G FILBEY		
	AMSRL WM MA		
	P MOY		
	AMSRL WM MC		
	J BEATTY		
	J MCCAULEY		
	R ADLER		
	M STAKER		
	E CHIN		
	J LASALVIA		
	AMSRL WM MD		
	R DOWDING		
	K CHO		

INTENTIONALLY LEFT BLANK

REPORT DOCUMENTATION PAGE			Form Approved OMB No. 0704-0188	
<small>Public reporting burden for this collection of information is estimated to average 1 hour per response, including the time for reviewing instructions, searching existing data sources, gathering and maintaining the data needed, and completing and reviewing the collection of information. Send comments regarding this burden estimate or any other aspect of this collection of information, including suggestions for reducing this burden, to Washington Headquarters Services, Directorate for Information Operations and Reports, 1215 Jefferson Davis Highway, Suite 1204, Arlington, VA 22202-4302, and to the Office of Management and Budget, Paperwork Reduction Project (0704-0188), Washington, DC 20503.</small>				
1. AGENCY USE ONLY (Leave blank)	2. REPORT DATE October 1998	3. REPORT TYPE AND DATES COVERED Final, Jan 93 - Sep 98		
4. TITLE AND SUBTITLE Shear and Axial Stress Response Under Fixed-End Forward/Reverse Torsion Loading of OFHC Copper		5. FUNDING NUMBERS 1L162618AH80		
6. AUTHOR(S) Tusit Weerasooriya				
7. PERFORMING ORGANIZATION NAME(S) AND ADDRESS(ES) U.S. Army Research Laboratory ATTN: AMSRL-WM-TD Aberdeen Proving Ground, MD 21005-5066		8. PERFORMING ORGANIZATION REPORT NUMBER ARL-TR-1828		
9. SPONSORING/MONITORING AGENCY NAMES(S) AND ADDRESS(ES)		10. SPONSORING/MONITORING AGENCY REPORT NUMBER		
11. SUPPLEMENTARY NOTES				
12a. DISTRIBUTION/AVAILABILITY STATEMENT Approved for public release; distribution is unlimited.			12b. DISTRIBUTION CODE	
13. ABSTRACT (Maximum 200 words) Torsion tests are conducted under fixed-end (axial constraint) conditions on thin tubular OFHC copper specimens. After a large shear strain of 2.2 in the forward direction, the specimen is twisted back to zero shear strain. From the tests, shear and axial stresses are obtained as a function of shear strain. These stress responses are also obtained from the Taylor-type polycrystal analysis with simple shear boundary conditions. Single-crystal constitutive parameters in the polycrystal analysis are obtained from uniaxial compressive tests conducted for large strains. Experimental and predicted torsion test results are compared. The Taylor method predicts the experimental shear stress response reasonably well under simple shear boundary conditions. Most of the salient features of the experimental axial stress response are captured by the Taylor prediction.				
14. SUBJECT TERMS polycrystal modeling, Taylor model, finite deformation, torsion, reverse loading, axial effects, OFHC copper			15. NUMBER OF PAGES 30	
			16. PRICE CODE	
17. SECURITY CLASSIFICATION OF REPORT UNCLASSIFIED	18. SECURITY CLASSIFICATION OF THIS PAGE UNCLASSIFIED	19. SECURITY CLASSIFICATION OF ABSTRACT UNCLASSIFIED	20. LIMITATION OF ABSTRACT UL	

INTENTIONALLY LEFT BLANK.

USER EVALUATION SHEET/CHANGE OF ADDRESS

This Laboratory undertakes a continuing effort to improve the quality of the reports it publishes. Your comments/answers to the items/questions below will aid us in our efforts.

1. ARL Report Number/Author ARL-TR-1828 (Weerasooriya) Date of Report October 1998

2. Date Report Received _____

3. Does this report satisfy a need? (Comment on purpose, related project, or other area of interest for which the report will be used.) _____

4. Specifically, how is the report being used? (Information source, design data, procedure, source of ideas, etc.) _____

5. Has the information in this report led to any quantitative savings as far as man-hours or dollars saved, operating costs avoided, or efficiencies achieved, etc? If so, please elaborate. _____

6. General Comments. What do you think should be changed to improve future reports? (Indicate changes to organization, technical content, format, etc.) _____

CURRENT
ADDRESS

Organization

Name

E-mail Name

Street or P.O. Box No.

City, State, Zip Code

7. If indicating a Change of Address or Address Correction, please provide the Current or Correct address above and the Old or Incorrect address below.

OLD
ADDRESS

Organization

Name

Street or P.O. Box No.

City, State, Zip Code

(Remove this sheet, fold as indicated, tape closed, and mail.)
(DO NOT STAPLE)